Journal of Computational Applied Mechanics 2023, 54(3): 347-364

DOI: 10.22059/JCAMECH.2023.361677.852

RESEARCH PAPER

Effect of higher order shear and normal deformable theory in buckling analysis of thick porous functionally graded plates

Elham Mohseni [a], Abusaleh Naderi[b,*]

[a] *Department of Mechanical Engineering, Shahid Bahonar University of Kerman, Kerman, Iran*
[b] *Department of Mechanical Engineering, Higher Education Complex of Bam, Bam, Iran*

Abstract

This paper presents an analytical solution for stability analysis of thick rectangular functionally graded plates with porosity subjected to in-plane loadings using the higher-order shear and normal deformable plate theory, for the first time. The plate material and its porosity are assumed to vary along the thickness direction. Also, three types of porosity pattern along the thickness direction are considered. Since the plate structure is not generally symmetry to the mid-plane it is assumed that the in-plane loads are applied to its neutral plane to remove the bending-stretching coupling. Stability equations are derived and then analytically solved for rectangular plates with simple supports using Legendre orthonormal polynomials and Navier's method to determine the critical buckling load. The results are then compared with estimates made using higher-order shear deformation (HSDT) and classical plate theories (CPT) available in the literature for FG non-porous plates. It is shown that compared to the HSDT, the HOSNDT yields smaller values for the plate critical buckling load and the effect of HOSNDT is more important as the plate thickness increases. In addition, it is demonstrated that compared to the uniaxial load, the effect of HOSNDT is greater as the plate is subjected to a biaxial compression load. Finally, the effects of the porosity distribution, porosity, power-law index, loading condition, and thickness ratio are studied in detail using HOSNDT. The results show that the porosity effect is greater in smaller values of the power-law index parameter.

Keywords: Higher order shear and normal deformations plate theory; Functionally graded porous materials; Thick rectangular plates; Legendre orthonormal polynomials; Stability analysis; Porosity effect.

1. Introduction

The fact that the material properties of functionally graded materials can be formed technologically to meet different performance requirements in different parts of a structural member is the basic advantage of those materials over common structural materials [1].

Functionally graded materials (FGMs) can be classified into different types based on the size and the structure [2, 3]. According to the thickness, these materials can be classified into thin and bulk FGMs. FGMs can also be classified as stepwise (or discontinuous) and continuous FGMs according to the type of grading [2, 4]. Conventional

* Corresponding author. Tel.: +983444020370.
E-mail address: : a.naderi@bam.ac.ir (Abusaleh Naderi)

functionally graded materials, constituted from two or more materials, are frequently used in various branches of practical engineering (such as aeronautics, nuclear reactors, electronics, biomedicine, and the automotive industry) because of their high durability, thermal resistance, corrosion resistance, flexibility, and toughness. However, there is another type of FGM that is graded in porosity or lattice structure [5, 6]. This type of FGM may have only one material and consequently the grading is represented by the gradually distributed porosity or lattice structure rather than the chemical composition [5, 6]. Also, it has been shown that common FGMs, having two or more material phase, can be further improved in terms of weight reduction and energy absorption by introducing the porosity while maintaining a significant amount of strength [7, 8]. Therefore, another type of FGMs can be that whose material and porosity distribution vary continuously in one or more direction.

Different techniques have been reported for manufacturing functionally graded porous materials. For example, functionally graded porous structures of acrylonitrile butadiene styrene have been fabricated with a solid-state constrained foaming process [7]. Continuous functionally graded porous scaffolds based on the Schwartz diamond unit cell with a wide range of graded volume fraction were manufactured by selective laser melting [9]. Functionally graded materials with porosity can also be manufactured by 3D printing technology. For example, Ozbolat and Khoda [10] designed a new parametric path plan for manufacturing of porous structures with functionally graded materials. They designed the interconnected and continuous deposition path to control the internal material composition in a functionally graded manner. Their proposed layer-based algorithmic solutions generate a bilayer pattern of zigzag and spiral toolpath consecutively to construct heterogeneous three-dimensional (3D) objects. In addition, different techniques have been reported for manufacturing porous materials by Goyal and Pandey [11], which some of them may be expanded to two phase materials.

Functionally graded materials with porosity have hopeful results for several engineering applications such as advanced refining [12], the automotive industry [13], and medical implants [9, 14].

Several researchers have investigated the mechanical responses of beams, plates and shells made from functionally graded porous materials. For example, Ebrahimi et al. [15] carried out thermo-mechanical vibration analyses of functionally graded beams made of porous material subjected to various thermal loadings. Rezaei et al. [16] investigated free vibration analysis of rectangular plates composed of functionally graded materials with porosities based on first-order shear deformation plate theory. Akbas [17] presented vibration analysis and static bending for a rectangular porous functionally graded plate with simple supports using the first-order shear deformation theory. Wang and Zhou [18] investigated large-amplitude vibration of sigmoid functionally graded thin plates with porosities. Their results indicate that the types of uniform and uneven porosity distributions have different effects on the resonance amplitude of the sigmoid functionally graded plate. Nam et al. [19] based on higher-order shear deformation theory studied buckling and post-buckling of stiffened porous functionally graded plate rested on Pasternak's elastic foundation. Zhao et al. [20] developed a new three-dimensional exact solution for vibration analysis of functionally graded porous thick plates with three different porosity distributions including even, uneven, and logarithmic-uneven. Ghorbanpour Arani et al. [21] studied free vibrations of rectangular plates made of porous materials in which Y-foam, G-foam, and Coustone are used. Enayat et al. [22] performed a comprehensive study of the mechanical behavior of functionally graded porous nanobeams resting on an elastic foundation. Rezaei and Saeedi [23] estimated the effect of the displacement coupling between solid and liquid on the free vibration characteristics of rectangular isotropic rigid porous plates under undrained conditions. They employed the Mindlin plate theory to model the moderately thick porous plate. Rezaei and Saidi [24] presented free vibrations of porous rectangular plates saturated with viscous fluid. Askari et al. [25] presented an exact Navier solution for free vibration analysis of thick rectangular FG porous plates surrounded by piezoelectric layers. They used third-order shear deformation plate theory and considered two different porosity distributions for the variation of mechanical properties of porous material across the thickness of the plate. Khorshidvand et al. [26] presented numerical solutions for static bending and mechanical buckling analysis of functionally graded porous plates. They modeled the problem based on a refined plate theory and considered three porosity distributions with the same total mass density. Kumar et al. [27] investigated the temperature-dependent vibration characteristics of FG porous plates using first-order shear deformation theory. Arefi et al. [28] studied size-dependent deflection analysis of FG graphene nanoplatelets reinforced composite micro-plates with porosity subjected to transverse load. They used third-order shear deformation theory of Reddy's. Radwan [29] investigated buckling and free vibration behaviors of functionally graded porous nanoplates embedded in an elastic medium are via a nonlocal strain gradient theory. Reddy and Reddy [30] investigated bending response of porous functionally graded plates using a higher order shear deformation theory. Zhou et al. [31] studied buckling analysis of functionally graded porous spherical caps reinforced by graphene platelets, including both symmetric and uniform porosity patterns in the metal matrix, together with five different graphene platelets distributions. Khatoonabadi et al. [32] investigated shear buckling

analysis of functionally graded porous annular sector plate reinforced with graphene nanoplatelets. They assumed that the plate is consisting of a layered model with uniform or non-uniform dispersion of graphene platelets in a metallic matrix including open-cell interior pores. Also, Asemi et al. [33] studied static, dynamic and natural frequency analyses of functionally graded porous annular sector plate reinforced by graphene nanoplatelets. They considered uniform and nonuniform dispersion of graphene platelets in a metallic matrix including open-cell interior pores. Arshid et al. [34] presented bending and buckling analyses of heterogeneous annular/circular micro sandwich plate located on Pasternak substrate. They assumed that the plate's core is made of saturated porous materials and face sheets are made of functionally graded piezo-electro-magnetic polymeric nano-composites. Khatounabadi et al. [35] resented the low-velocity impact analysis of functionally graded porous circular plate reinforced with graphene platelets based on the first-order shear deformation theory. Babaei et al. [36] reviewed the mechanical properties of functionally graded saturated porous structures and presented a comprehensive review on the mechanical analyses of these structures in saturated condition. Also, they discussed the challenges and possible future works on this area. Alhaifi [37] investigated large deflection analysis of a functionally graded saturated porous rectangular plate subjected to transverse loading which is located on a nonlinear three-parameter elastic foundation. Babaei and Asemi [38] studied static response of functionally graded saturated porous rotating truncated cone is investigated. They considered three different patterns for porosity distribution along with the thickness of the cone. Babaei et al. [39] studied an axisymmetric rotating truncated cone made of functionally graded porous materials reinforced by graphene platelets under a thermal loading.

It should be noted that functionally graded porous plates can generally be categorized into two different classes: a) those that are made from a single material phase and have a variable porosity distribution in at least one direction (i.e. homogenous ones), and b) those that consist of two material phases and have a uniform or non-uniform pattern of the porosity distribution (i.e. inhomogeneous ones). To the best of the authors' knowledge, the researches on static, buckling and vibration analyses of homogeneous and inhomogeneous functionally graded porous plates have been performed based on common plate theories such as classical, first order shear deformation and higher order shear deformation theories. In general, the plate problems can be solved by using 3D elasticity theory or common plate theories. However, compared to the 3D elasticity theory, solving the plate problems based on the plate theories is more convenient. Nevertheless, because of some simplifying assumptions on the plate deformations (for example, ignoring some deformations and choosing some predefined patterns for the deformations) the common plate theories (such as classical plate theory, first-order shear deformation theory, higher order shear deformation theories, and etc.) are not as accurate as the 3D elasticity theory, especially for thick plates. However, the higher-order shear and normal deformable theory not only considers all possible deformations of the plate, but also does not use a predefined pattern for the plate deformations. So, this theory can cause results with the same degree of accuracy as the 3D elasticity theory. Also, this theory is more convenient than the 3D elasticity theory, especially for thick plates due to its two-dimensional form. Therefore, in general, the higher-order shear and normal deformable theory can be preferred over the 3D elasticity theory.

The above literature review indicates that the buckling analysis of functionally graded plates with porosity using the higher-order shear and normal deformable theory has not been investigated yet and the only published work on this area refers to the buckling analysis of functionally graded porous plates reinforced by orthogonal and/or oblique stiffeners based on the higher-order shear deformation theory performed by Nam et al. [19]. Therefore, this paper aims to investigate the effect of porosity on the buckling behaviour of thick plates made of functionally materials using the higher-order shear and normal deformable theory. The plate material and the porosity are considered to vary through the plate thickness direction according to, respectively, a power-law function and a cosine function. Also, three types of porosity gradation along the thickness are considered. Since the plate structure is not symmetry to the mid-plane, it is assumed that the plate is under in-plane loading on its neutral plane which is at a definite distance from the mid-plane [40]. The position of the neutral plane of the porous FG plate is determined. Stability equations are derived and then analytically solved to find the critical buckling load. The results are then compared to those obtained from common plate theories. Finally, the effects of the theory, porosity distribution function, porosity, power-law index, loading condition, and thickness ratio on the plate critical buckling load are studied in detail. In addition, the physical reasons for each finding are discussed in detail. The exact analytical results can be used as a benchmark solution for future numerical analysis.

2. Material properties

Consider a rectangular porous FG plate whose material and porosity distributions vary continuously along the thickness direction, as shown in Figure 1. Because of the isotropic behavior of its material, the constitutive relation for such plate is written as

$$\sigma_{ij} = 2\mu\varepsilon_{ij} + \lambda\varepsilon_{kk}\delta_{ij} \tag{1}$$

where $\sigma_{ij}(i, j = 1,2,3)$ and ε_{ij} are, respectively, stress and strain components. Also, δ_{ij} is the Kroncker delta function, and λ and μ are Lamè constants, expressed in terms of the engineering constants in the following form

$$\lambda = \frac{E\nu}{(1+\nu)(1-2\nu)}, \quad \mu = \frac{E}{2(1+\nu)} \tag{2}$$

where E is the Young's modulus and ν is the Poisson's ratio.

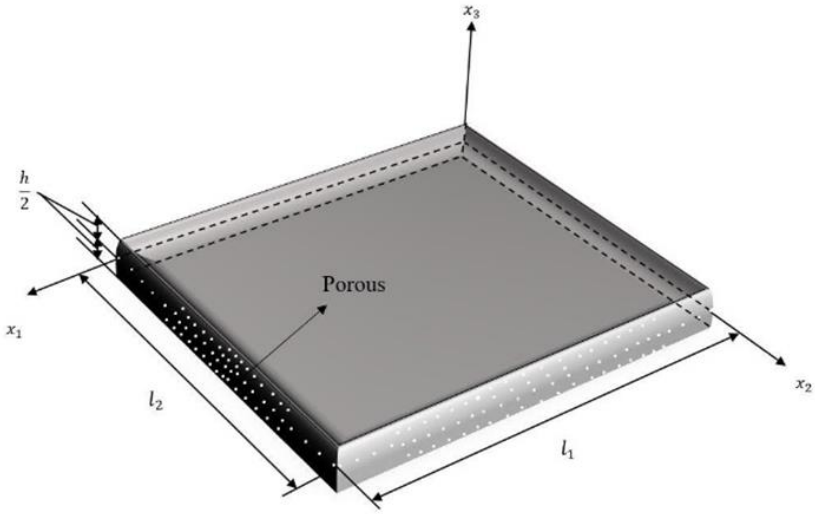

Fig 1. Schematic of rectangular porous FG plate

The material distribution and the porosity distribution are considered to vary according to, respectively, a power law function and a trigonometric function. Therefore, a typical material property for such a plate can be expressed in terms of the thickness direction as follows [41, 42]

$$H(x_3) = \left((H_c - H_m)\left(\frac{1}{2} + \frac{x_3}{h}\right)^N + H_m \right)(1 - \psi(x_3)) \tag{3}$$

where H is a typical material property of the plate, (e.g. Young's modulus E). Also, H_c and H_m are material properties of the plate, respectively, at $x_3 = h/2$ and $x_3 = -h/2$. Here, since the variation of the Poisson's ratio through the thickness is relatively small, it is conveniently considered to be constant [30, 41]. Moreover, in equation (3) the function $\psi(x_3)$ is the porosity distribution function which can be written as the following relations [42]

$$\text{Type1: } \psi(x_3) = \varphi\cos\left(\frac{\pi x_3}{h}\right) \tag{4-1}$$

$$\text{Type 2: } \psi(x_3) = \varphi\cos\frac{\pi}{2}\left(\frac{x_3}{h} + \frac{1}{2}\right) \tag{4-2}$$

$$\text{Type 3: } \psi(x_3) = \varphi\cos\frac{\pi}{2}\left(\frac{x_3}{h} - \frac{1}{2}\right) \tag{4-3}$$

where φ indicates the porosity coefficient. Figure 2 depicts the normalized porosity distribution functions versus the thickness-direction coordinate. This figure shows that based on the distribution function of type 1, the porosity is

symmetric to the mid-plane, and also the central part of the plate is more porous. This figure also shows that for plates with a distribution function of type 2, the porosity increases from the upper surface to the lower surface. The inverse pattern is observed for type 3 of the porosity distribution function.

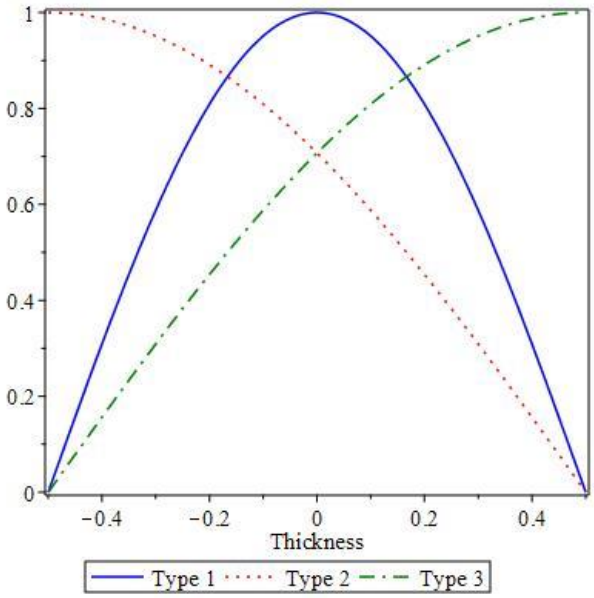

Fig 2. The normalized porosity distribution functions $\bar{\psi}(x_3)=\dfrac{\psi(x_3)}{\phi}$

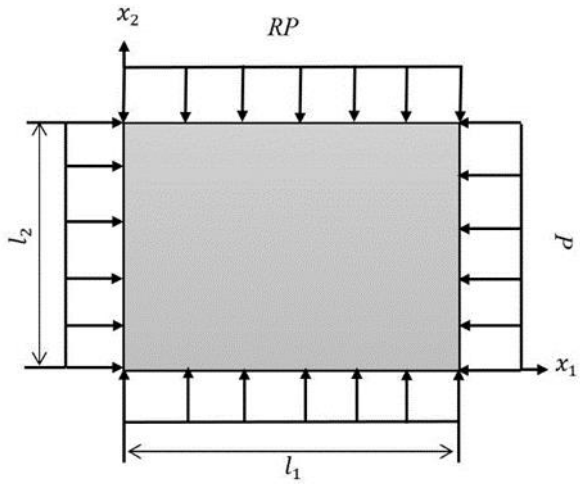

Fig 3. Schematic of the rectangular porous FG plate under in-plane loading

3. Loading conditions

As shown in Figure 3, the plate is assumed to be under in-plane uniaxial compressive ($R=0$), in-plane biaxial compressive ($R=1$), or tension-compression biaxial ($R=-1$) loading. It can be seen from Eq. (3) together with Eqs. (4) that the plate structure is not symmetry concerning the mid-plane. Consequently, because of bending-stretching coupling, the plate will bend under any in-plane load, unless the loads (load per unit length) are applied along with its neutral plane. Therefore, since the buckling analysis is under investigation, it is considered here that the plate is under in-plane loads in the neutral plane of the plate [40].

4. Nonlinear equilibrium equations

Equilibrium equations are derived here based on the geometrical nonlinearity assumptions of Von Karman. To this end, higher-order shear and normal deformable plate theory (HOSNDT) is chosen because, contrary to other plate theories, it considers all possible plate deformation and does not use a predefined pattern for the plate deformations. According to this theory, displacement components of the plate are expanded in terms of Legendre orthonormal polynomials in the thickness direction as follows [43]

$$u_1(x_1,x_2,x_3,t)=u(x_1,x_2,x_3,t)=\sum_{a=0}^{K}L_a(x_3)u^a(x_1,x_2,t) \tag{5-1}$$

$$u_2(x_1,x_2,x_3,t)=v(x_1,x_2,x_3,t)=\sum_{a=0}^{K}L_a(x_3)v^a(x_1,x_2,t) \tag{5-2}$$

$$u_3(x_1,x_2,x_3,t)=w(x_1,x_2,x_3,t)=\sum_{a=0}^{K}L_a(x_3)w^a(x_1,x_2,t) \tag{5-3}$$

in which $L_a(x_3)$ denotes Legendre polynomial functions generally defined in terms of the basic functions $1, x_3, x_3^2, x_3^3, \ldots$. For example, some of these polynomials are presented here as follows

$$L_0(x_3)=\frac{\sqrt{2}}{2}, L_1(x_3)=\frac{\sqrt{6}}{2}x_3, L_2(x_3)=\frac{\sqrt{10}}{2}(-\frac{1}{2}+\frac{3}{2}x_3^2), L_3(x_3)=\frac{\sqrt{14}}{2}(\frac{5}{2}x_3^3-\frac{3}{2}x_3)$$
$$, L_4(x_3)=\frac{3\sqrt{2}}{2}(\frac{35}{8}x_3^4-\frac{15}{4}x_3+\frac{3}{8}), L_5(x_3)=\frac{\sqrt{22}}{2}(\frac{63}{8}x_3^5-\frac{35}{4}x_3^3+\frac{15}{8}x_3) \tag{6}$$

Generally, for $K \geq 2$, the plate theory is called high-order. It can be easily shown that the above functions satisfy the orthogonal property in the following form

$$\int_{-1}^{1} L_a(x_3)L_b(x_3)dx_3=\delta_{ab} \qquad a,b=0,1,...,K \tag{7}$$

where δ_{ab} is Kronecker Delta. Also, the derivative of Legendre polynomials can be expressed as

$$L_a'(x_3)=D_{ab}L_b(x_3)=\sum_{b=0}^{K=5} D_{ab}L_b(x_3) \tag{8}$$

where, D_{ab} are constant coefficients which can be written for $K=5$ in the following matrix form

$$[D]_{7\times 7}=\begin{bmatrix} 0 & 0 & 0 & 0 & 0 & 0 & 0 & 0 \\ \sqrt{3} & 0 & 0 & 0 & 0 & 0 & 0 & 0 \\ 0 & \sqrt{15} & 0 & 0 & 0 & 0 & 0 & 0 \\ \sqrt{7} & 0 & \sqrt{35} & 0 & 0 & 0 & 0 & 0 \\ 0 & 3\sqrt{3} & 0 & 3\sqrt{7} & 0 & 0 & 0 & 0 \\ \sqrt{11} & 0 & \sqrt{35} & 0 & 3\sqrt{11} & 0 & 0 & 0 \\ 0 & \sqrt{39} & 0 & \sqrt{91} & 0 & \sqrt{143} & 0 & 0 \\ \sqrt{15} & 0 & 5\sqrt{3} & 0 & 3\sqrt{15} & 0 & \sqrt{195} & 0 \end{bmatrix} \tag{9}$$

It should be noted that generally there is no limitation on the value of K. Based on the geometrical nonlinearity assumptions of Von Karman, together with the relations in Eq. (5), one can write [44]

$$\begin{Bmatrix} \varepsilon_{11} \\ \varepsilon_{22} \\ \varepsilon_{33} \\ \gamma_{12} \\ \gamma_{13} \\ \gamma_{23} \end{Bmatrix}=\begin{Bmatrix} \frac{\partial u}{\partial x_1}+\frac{1}{2}(\frac{\partial w}{\partial x_1})^2 \\ \frac{\partial v}{\partial x_2}+\frac{1}{2}(\frac{\partial w}{\partial x_2})^2 \\ \frac{\partial w}{\partial x_3}+\frac{1}{2}(\frac{\partial w}{\partial x_3})^2 \\ \frac{\partial u}{\partial x_2}+\frac{\partial v}{\partial x_1}+\frac{\partial w}{\partial x_1}\frac{\partial w}{\partial x_2} \\ \frac{\partial u}{\partial x_3}+\frac{\partial w}{\partial x_1}+\frac{\partial w}{\partial x_1}\frac{\partial w}{\partial x_3} \\ \frac{\partial v}{\partial x_3}+\frac{\partial w}{\partial x_2}+\frac{\partial w}{\partial x_2}\frac{\partial w}{\partial x_3} \end{Bmatrix}=\begin{Bmatrix} L_a(x_3)u_{,1}^a+\frac{1}{2}L_a(x_3)L_b(x_3)w_{,1}^a w_{,1}^b \\ L_a(x_3)v_{,2}^a+\frac{1}{2}L_a(x_3)L_b(x_3)w_{,1}^a w_{,1}^b \\ D_{ab}L_b(x_3)w^a+\frac{1}{2}D_{ab}L_b(x_3)D_{cd}L_d(x_3)w^a w^c \\ L_a(x_3)u_{,2}^a+L_a(x_3)v_{,1}^a+L_a(x_3)L_b(x_3)w_{,1}^a w_{,2}^b \\ D_{ab}L_b(x_3)u^a+L_a(x_3)w_{,1}^a+L_a(x_3)D_{bc}L_c(x_3)w_{,1}^a w^b \\ D_{ab}L_b(x_3)v^a+L_a(x_3)w_{,2}^a+L_a(x_3)D_{bc}L_c(x_3)w_{,2}^a w^b \end{Bmatrix} \tag{10}$$

Equilibrium equations are derived using the minimum total potential energy $(\delta(U+W)=0)$. To this end, variations of the strain energy and the potential energy of the external loads are written as follows

$$\begin{aligned}\delta U &= \int_{\Omega}\int_{-\frac{h}{2}}^{\frac{h}{2}}(\sigma_{11}\delta\varepsilon_{11}+\sigma_{22}\delta\varepsilon_{22}+\sigma_{33}\delta\varepsilon_{33}+\sigma_{12}\delta\gamma_{12}+\sigma_{13}\delta\gamma_{13}+\sigma_{23}\delta\gamma_{23})dx_1dx_2dx_3\\ \delta W &= \int_S(-PL_a(e)\delta v_1^a - RPL_a(e)\delta v_2^a)dS\end{aligned} \tag{11}$$

where, e is the distance of the neutral plane from the mid-plane, which is determined in the next section. Upon substituting equation (10) into equation (11-1), one can obtain

$$\begin{aligned}\delta U = \int_{\Omega}\int_{-\frac{h}{2}}^{\frac{h}{2}}[&\sigma_{11}(L_a(x_3)\delta u_{,1}^a + L_a(x_3)L_b(x_3)w_{,1}^b\delta w_{,1}^a)\\ &+\sigma_{22}(L_a(x_3)\delta v_{,2}^a + L_a(x_3)L_b(x_3)w_{,2}^b\delta w_{,2}^a)+\sigma_{33}(D_{ab}L_b(x_3)\delta w^a + D_{ab}L_b(x_3)D_{cd}L_d(x_3)w^c\delta w^a)\\ &+\sigma_{12}(L_a(x_3)\delta u_{,2}^a + L_a(x_3)\delta v_{,1}^a + L_a(x_3)L_b(x_3)w_{,2}^b\delta w_{,1}^a + L_a(x_3)L_b(x_3)w_{,1}^b\delta w_{,2}^a)\\ &+\sigma_{13}(D_{ab}L_b(x_3)\delta u^a + L_a(x_3)\delta w_{,1}^a + L_a(x_3)D_{bc}L_c(x_3)w^b\delta w_{,1}^a + L_a(x_3)D_{bc}L_c(x_3)w_{,1}^b\delta w^a)\\ &+\sigma_{23}(D_{ab}L_b(x_3)\delta v^a + L_a(x_3)\delta w_{,2}^a + L_a(x_3)D_{bc}L_c(x_3)w^b\delta w_{,2}^a + L_a(x_3)D_{bc}L_c(x_3)w_{,2}^b\delta w^a)]dx_1dx_2dx_3\end{aligned} \tag{12}$$

By introducing the following normal and shear stress resultants

$$M_{\alpha\beta}^{a} = \int_{-\frac{h}{2}}^{\frac{h}{2}}\sigma_{\alpha\beta}L_a(x_3)dx_3 \tag{13-1}$$

$$M_{\alpha\beta}^{ab} = \int_{-\frac{h}{2}}^{\frac{h}{2}}\sigma_{\alpha\beta}L_a(x_3)L_b(x_3)dx_3 \tag{13-2}$$

$$T_i^a = \int_{-\frac{h}{2}}^{\frac{h}{2}}\sigma_{i3}L_a(x_3)dx_3 \tag{13-3}$$

$$T_i^{ab} = \int_{-\frac{h}{2}}^{\frac{h}{2}}\sigma_{i3}L_a(x_3)L_b(x_3)dx_3 \tag{13-4}$$

variation of the strain energy in Eq. (12) can be rewritten in the following form

$$\begin{aligned}\delta U = \int_{\Omega}[&(M_{11}^a\delta u_{,1}^a + M_{11}^{ab}w_{,1}^b\delta w_{,1}^a + M_{22}^a\delta v_{,2}^a + M_{22}^{ab}w_{,2}^b\delta w_{,2}^a\\ &+T_{33}^bD_{ab}\delta w^a + T_{33}^{bd}D_{ab}D_{cd}w^c\delta w^a\\ &+M_{12}^a\delta u_{,2}^a + M_{12}^a\delta v_{,1}^a + M_{12}^{ab}w_{,2}^b\delta w_{,1}^a + M_{12}^{ab}w_{,1}^b\delta w_{,2}^a\\ &+T_1^bD_{ab}\delta u^a + T_1^a\delta w_{,1}^a + T_1^{ac}D_{bc}w^b\delta w_{,1}^a + T_1^{ac}D_{bc}w_{,1}^a\delta w^b\\ &+T_2^bD_{ab}\delta v^a + T_2^b\delta w_{,2}^a + T_2^{ac}D_{bc}w^b\delta w_{,2}^a + T_2^{ac}D_{bc}w_{,2}^a\delta w^b)]dx_1dx_2dx_3\end{aligned} \tag{14}$$

According to the minimum total potential energy, the equilibrium equations can be obtained as follows [44]

$$\delta u^a : (T_1^bD_{ab} - \frac{\partial M_{11}^a}{\partial x_1} - \frac{\partial M_{12}^a}{\partial x_2}) = 0 \tag{15-1}$$

$$\delta v^a : (T_2^bD_{ab} - \frac{\partial M_{12}^a}{\partial x_1} - \frac{\partial M_{22}^a}{\partial x_2}) = 0 \tag{15-2}$$

$$\delta w^a : (T_3^b D_{ab} - \frac{\partial T_1^a}{\partial x_1} - \frac{\partial T_2^a}{\partial x_2} - (M_{11}^{ab} w_{,1}^b)_{,1} - (M_{22}^{ab} w_{,2}^b)_{,2} + T_{33}^{bd} D_{ab} D_{cd} w^c - (M_{12}^{ab} w_{,2}^b)_{,1} \\ - (M_{12}^{ab} w_{,1}^b)_{,2} - (T_1^{ac} D_{bc} w^b)_{,1} + T_1^{bc} D_{ac} w_{,1}^b - (T_2^{ac} D_{bc} w^b)_{,2} + T_2^{bc} D_{ac} w_{,2}^b = 0 \tag{15-3}$$

Also, the plate boundary conditions are obtained in the form [44]

$$\delta u^a : (M_{11}^a - PL_a(e))\mathbf{n}_1 + (M_{12}^a)\mathbf{n}_2 = 0 \tag{16-1}$$

$$\delta v^a : (M_{12}^a)\mathbf{n}_1 + (M_{22}^a - RPL_a(e))\mathbf{n}_2 = 0 \tag{16-3}$$

$$\delta w^a : (T_1^a + M_{11}^{ab} w_{,1}^b + M_{12}^{ab} w_{,2}^b + T_1^{ac} D_{bc} w^b)\mathbf{n}_1 + (T_2^a + M_{22}^{ab} w_{,2}^b + M_{12}^{ab} w_{,1}^b + T_2^{ac} D_{bc} w^b)\mathbf{n}_2 = 0 \tag{16-4}$$

where, $\mathbf{n}_1$ and $\mathbf{n}_2$ are unit outward normal vectors in the x_1 - and x_2 - directions, respectively. It should be noted that the stress and moment resultants $M_{\alpha\beta}^a$, $M_{\alpha\beta}^{ab}$, T_i^a, and T_i^{ab} can easily be written in terms of the displacement components u^a, v^a, w^a upon using relations (1), (5), (10), and (13).

5. Distance of the neutral plane from the mid-plane

As mentioned earlier, in order to have essentially a buckling problem for the FG plates whose material properties vary continuously along the thickness direction, the external in-plane loads should be applied to the neutral plane, which is not generally the mid-plane (unless the plate material is symmetric to the mid-plane). If the in-plane loads are exerted on a different position, because of the bending-stretching coupling, the plate will bend immediately under any in-plane load and consequently it cannot sustain any in-plane load without bending. Therefore, the critical buckling load can be obtained only for the case of that assumption.

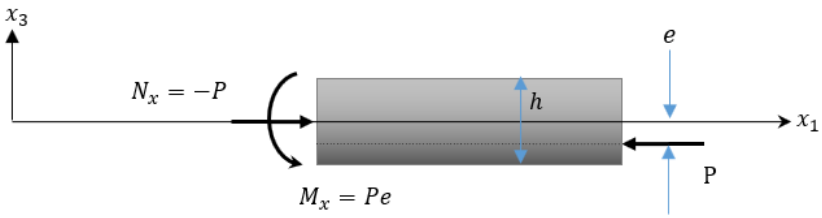

Figure 4. Uniaxial in-plane compressive load P on the neutral plane

In order to find the position of the neutral plane, for example, consider the plate is under uniaxial in-plane compressive load P on its neutral plane located at a distance e from the mid-plane (as shown in Fig 4). Consequently, the plate will remain flat before the buckling occurs. In other words, the plate deflection will be zero ($w = 0$) before buckling. Clearly, the internal force and moments on the mid-plane at any section perpendicular to the x_1 axis can be expressed as

$$N_x = -P \tag{17-1}$$

$$M_x = Pe \tag{17-2}$$

where

$$N_x = \int_{-\frac{h}{2}}^{\frac{h}{2}} \sigma_{11} dx_3 \tag{18-1}$$

$$M_x = \int_{-\frac{h}{2}}^{\frac{h}{2}} \sigma_{11} x_3 dx_3 \tag{18-2}$$

Upon using Eqs. (1) and (10), and satisfying the condition $w=0$, the stress component σ_{11} in the pre-buckling configuration can be expresses in the form

$$\sigma_{11}=\left(\lambda+2\mu\right)L_0\left(x_3\right)u_{,1}^0+\lambda L_0\left(x_3\right)v_{,2}^0 \tag{19}$$

Substituting the above equation into relations (18-1) and (18-2), yields

$$N_x=A_{11}u_{,1}^0+A_{12}v_{,2}^0 \tag{20-1}$$

$$M_x=B_{11}u_{,1}^0+B_{12}v_{,2}^0 \tag{20-2}$$

where

$$A_{11}=\int_{-\frac{h}{2}}^{\frac{h}{2}}\left(\lambda+2\mu\right)L_0\left(x_3\right)dx_3 \tag{21-1}$$

$$A_{12}=\int_{-\frac{h}{2}}^{\frac{h}{2}}\lambda L_0\left(x_3\right)dx_3 \tag{21-2}$$

$$B_{11}=\int_{-\frac{h}{2}}^{\frac{h}{2}}x_3\left(\lambda+2\mu\right)L_0\left(x_3\right)dx_3 \tag{21-3}$$

$$B_{12}=\int_{-\frac{h}{2}}^{\frac{h}{2}}x_3\lambda L_0\left(x_3\right)dx_3 \tag{21-4}$$

Upon substituting Eqs. 2 into relations (21), it can be easily show that

$$A_{12}=\frac{\nu}{1-\nu}A_{11} \tag{22-1}$$

$$B_{12}=\frac{\nu}{1-\nu}B_{11} \tag{22-2}$$

Substitution relations (22) and (17) into relations (20), the distance e is obtained in the following form [40]

$$e=-\frac{B_{11}}{A_{11}} \tag{23}$$

Also, the above relation can be written in terms of the Young's modulus in the following form

$$e=-\frac{A_{11}=\int_{-\frac{h}{2}}^{\frac{h}{2}}x_3E\left(x_3\right)dx_3}{B_{11}=\int_{-\frac{h}{2}}^{\frac{h}{2}}E\left(x_3\right)dx_3} \tag{24}$$

6. Stability equations

Stability equations are derived here using the adjacent equilibrium criterion. Consider the plate subjected to the compressive in-plane loading is under the neutral equilibrium configuration. Consequently, the plate will have another equilibrium configuration in the vicinity of the first equilibrium state and the loads are in fact the critical

buckling loads. Therefore, to derive the stability equations, a displacement field is introduced in the vicinity of the initial equilibrium state in the form

$$u^a = \bar{u}^a + \tilde{u}^a \tag{25-1}$$

$$v^a = \bar{v}^a + \tilde{v}^a \tag{25-2}$$

$$w^a = \bar{w}^a + \tilde{w}^a \tag{25-3}$$

where, $\bar{u}^a, \bar{v}^a, \bar{w}^a$ refer to the initial equilibrium state and $\tilde{u}^a, \tilde{v}^a, \tilde{w}^a$ are the corresponding incremental displacements from the initial state.

By substituting Eqs. (25) into Eqs. (13), the stress resultants in the new equilibrium state are obtained as

$$M^a_{\alpha\beta} = \bar{M}^a_{\alpha\beta} + \tilde{M}^a_{\alpha\beta} \tag{26-1}$$

$$M^{ab}_{\alpha\beta} = \bar{M}^{ab}_{\alpha\beta} + \tilde{M}^{ab}_{\alpha\beta} \tag{26-2}$$

$$T^a_i = \bar{T}^a_i + \tilde{T}^a_i \tag{26-3}$$

$$T^{ab}_i = \bar{T}^{ab}_i + \tilde{T}^{ab}_i \tag{26-4}$$

By replacing Eqs. (26) into the nonlinear equilibrium equations (15), and satisfying the equations for the initial equilibrium state, also ignoring the nonlinear incremental small terms, the stability equations are obtained as follows [44]

$$\delta u^a : (\tilde{T}^b_1 D_{ab} - \frac{\partial \tilde{M}^a_{11}}{\partial x_1} - \frac{\partial \tilde{M}^a_{12}}{\partial x_2}) = 0 \tag{27-1}$$

$$\delta v^a : (\tilde{T}^b_2 D_{ab} - \frac{\partial \tilde{M}^a_{12}}{\partial x_1} - \frac{\partial \tilde{M}^a_{22}}{\partial x_2}) = 0 \tag{27-2}$$

$$\delta w^a : (\tilde{T}^b_3 D_{ab} - \frac{\partial \tilde{T}^a_1}{\partial x_1} - \frac{\partial \tilde{T}^a_2}{\partial x_2} - \bar{M}^{ab}_{11} \tilde{w}^b_{,11} - \bar{M}^{ab}_{22} \tilde{w}^b_{,22}) = 0 \tag{27-3}$$

where $\bar{M}^{ab}_{11}$ and $\bar{M}^{ab}_{22}$ are defined in terms of the external in-plane load parameter P. The stability boundary conditions are also obtained by using the vicinity equilibrium criterion as follows

$$\delta u^a : (\tilde{M}^a_{11})\mathbf{n}_1 + (\tilde{M}^a_{12})\mathbf{n}_2 = 0 \tag{28-1}$$

$$\delta v^a : (\tilde{M}^a_{12})\mathbf{n}_1 + (\tilde{M}^a_{22})\mathbf{n}_2 = 0 \tag{28-2}$$

$$\delta w^a : (\tilde{T}^a_1 + \bar{M}^{ab}_{11} \tilde{w}^b_{,1})\mathbf{n}_1 + (\tilde{T}^a_2 + \bar{M}^{ab}_{22} \tilde{w}^b_{,2})\mathbf{n}_2 = 0 \tag{28-3}$$

It should be noted that the incremental stress and moment resultants $\tilde{M}^a_{\alpha\beta}$, $\tilde{M}^{ab}_{\alpha\beta}$, $\tilde{T}^a_i$, and $\tilde{T}^{ab}_i$ can easily be written in terms of the incremental displacements $\tilde{u}^a, \tilde{v}^a, \tilde{w}^a$ upon using relations (1), (5), (10) and (25). Therefore, the stability equations (27) together with the stability boundary conditions (28) can be expressed generally in terms of the incremental displacements $\tilde{u}^a, \tilde{v}^a, \tilde{w}^a$. Generally, solving a system of highly coupled differential equation with

variable coefficient requires numerical method. However, for some especial cases, for example, for plates with all edges simply supported those equations can be solved analytically and the exact analytical solutions can be obtained, which can be used as a benchmark solution for future numerical studies.

7. Solution procedure

It is assumed that the plate has simple supports along all edges, so the stability boundary conditions of the plate can be written in the form

$$on\, x_1 = 0\, and\, x_1 = l_1 \Rightarrow W^a = 0, M_{11}^a = 0, M_{21}^a = 0 \tag{29-1}$$

$$on\, x_2 = 0\, and\, x_2 = l_2 \Rightarrow W^a = 0, M_{22}^a = 0, M_{12}^a = 0 \tag{29-2}$$

According to the above boundary conditions, the solution of the stability equations (27) can be written in the following series form

$$\tilde{u}^a(x_1, x_2, t) = \sum_{m,n=1} \tilde{U}^{amn}(t) \cos(\frac{m\pi x_1}{l_1}) \sin(\frac{n\pi x_2}{l_2}) \tag{30-1}$$

$$\tilde{v}^a(x_1, x_2, t) = \sum_{m,n=1} \tilde{V}^{amn}(t) \sin(\frac{m\pi x_1}{l_1}) \cos(\frac{n\pi x_2}{l_2}) \tag{30-2}$$

$$\tilde{w}^a(x_1, x_2, t) = \sum_{m,n=1} \tilde{W}^{amn}(t) \sin(\frac{m\pi x_1}{l_1}) \sin(\frac{n\pi x_2}{l_2}) \tag{30-3}$$

in which, $\tilde{U}^{amn}$, $\tilde{V}^{amn}$, and $\tilde{W}^{amn}$ are some constant coefficients. Also, m and n are the half-wave numbers. Substitution of Eqs. (30) into the stability equations (27) gives an Eigenvalue problem to find the critical buckling load P .

8. Numerical results and discussions

In this section, the critical buckling load is obtained for functionally gradated rectangular porous plates according to the higher-order shear and normal deformable plate theory. Also, to validate the study, the results are compared with those reported in previous works. In addition, the effects of different material and geometrical parameters on the plate buckling behaviour are studied in detail.

In order to determine the critical buckling load, minimum magnitude of the buckling load P should be sought for different values of the Legendre polynomial number ($a = 0,1,2,3,...,K$) and the mode numbers m and n ($m,n = 1,2,3,...$). Generally, there is no limitation on the number of the Legendre polynomials (K). However, usually the critical buckling load occurs for $a < 6$. Therefore, seven Legendre polynomials and consequently seven terms of the series solutions are sufficient for finding the critical buckling load.

Table 1. Comparison of the dimensionless critical buckling load parameter $\tilde{P}_{cr} = P_{cr} \times 10^{-6} / l_2$ of a rectangular porous FG plate with refs [44] and [45] ($h/l_2 = 0.1$ and $\varphi = 0$)

N	R	l_1/l_2	*Present Study*	[43] (HOSNDT)	[44] (HSDT)
0	1	1	715.797(1)	715.808(1)	718.692(1)
		1.5	525.308(1)	525.308(1)	526.861(1)
	0	1	1431.595(1)	1431.594(1)	1437.361(1)
		1.5	1519.588(2)	1519.588(2)	1527.903(2)
	-1	1	2746.838(2)	2746.842(2)	2772.980(2)
		1.5	2746.838(3)	2746.842(3)	2772.980(3)
1	1	1	350.034(1)	350.034(1)	351.124(1)
		1.5	256.194(1)	256.194(1)	256.776(1)
	0	1	700.068(1)	700.068(1)	702.304(1)
		1.5	745.802(2)	745.801(2)	748.920(2)
	-1	1	1361.175(2)	1361.174(2)	1371.653(2)
		1.5	1361.175(3)	1361.174(3)	1371.653(3)

Superscript numbers in parentheses indicate the buckling load mode number

Table 1 compares the results of this study for $\varphi = 0$ with those reported in Refs. [44] and [45]. As can be seen from this table, the presented results are in excellent agreement with those reported in Ref. [44] based on the higher-order shear and normal deformable theory (HOSNDT). However, these results differ from those obtained according to higher-order shear deformation theory (HSDT) reported in Ref. [45]. This difference, however, refers to the fact that the HOSNDT takes into account normal deformations across the thickness, which results in a reduction in plate stiffness and hence in the critical buckling load. Also, this table indicates that the effect of HOSNDT for $l_1/l_2 = 1$ is greater than for $l_1/l_2 = 1.5$, which means that as plate stiffness increases, the effect of HOSNDT increases.

Table 2. Comparison of the dimensionless critical buckling load parameter $\hat{P}_{cr} = P_{cr} 12 l_1^2 (1-\nu^2)/Eh^3$ of a square porous FG plate for $\varphi = 0$ with those reported in Ref. [46]

R	N	$h/l_1 = 0.01$		$h/l_1 = 0.02$		$h/l_1 = 0.03$	
		Present Study	Ref. [45]	*Present Study*	Ref. [45]	*Present Study*	Ref. [45]
0	0	1.1244	1.1222	8.9804	8.9104	30.2259	30.072
	1	0.9315	0.95022	7.4392	7.6018	25.0351	25.656
	2	0.8939	0.89103	7.1378	7.1283	24.0160	24.058
	5	0.8599	0.82293	6.8496	6.5834	23.0417	22.219
1	0	0.5622	0.55692	4.4902	4.4552	15.1130	15.036
	1	0.4658	0.44605	3.7196	3.6845	12.5175	12.435
	2	0.4469	0.44329	3.5689	3.5463	12.0080	11.969
	5	0.3920	0.42712	3.4248	3.4168	11.5209	11.532

Table 2 compares the critical buckling load parameter $\hat{P}_{cr} = P_{cr} 12 l_1^2 (1-\nu^2)/Eh^3$ for different power-law indices, load parameters, and thickness ratio values to those reported in Ref. [46] using the classical plate theory. This table reveals that as the thickness parameter is increased, the effect of HOSNDT increases. Moreover, it can be seen from this table that for thin plates, there is no considerable difference between the results of two theories. In addition, this table indicates that compared with the uniaxial loading, the effect of HOSNDT is more significant for biaxial loading. This issue, however, refers to the fact that normal deformations are more significant when the plate is subjected to biaxial compressive loading.

Table 3. Material properties

Epoxy 1	$E_m = 1.44 \times 10^9\ N/m^2$	$\nu_m = 0.38$
Epoxy 2	$E_c = 14.4 \times 10^9\ N/m^2$	$\nu_c = 0.38$

The results are presented here, for porous FG plates constructed from the materials listed in Table 3. Moreover, the critical buckling load is presented in the following non-dimensional form.

$$\bar{P}_{cr} = \frac{P_{cr} l_2^2}{Eh^3} \tag{31}$$

Table 4 shows the effects of the porosity distribution, thickness ratio l_1/h, power-law index N, and porosity φ on the critical buckling load parameter $\bar{P}_{cr}$ for a square porous FG plate. As can be seen from this table, the dimensionless critical buckling load $\bar{P}_{cr}$ increases with increasing the thickness ratio l_1/h. This issue, however, refers to the fact that according to Eq. (31), the buckling load is dimensionless with respect to the function h^3 and also the growth of the denominator and the numerator with respect to h (or h/l) is not the same. Therefore, although the plate stiffness and consequently the buckling load decrease with increasing the length to thickness ratio, it is observed that the non-dimensional form of the buckling load decreases. Also, this table illustrates that as the value of the power-law index N increases, the critical buckling load decreases. This issue refers to the fact that with the increase in its value, the volume fracture of the material with smaller Young's modulus (E_m) increases and consequently the stiffness of the plate decreases. Therefore, the more value for N, the less value for $\bar{P}_{cr}$. Furthermore, it is observed from the results of this table that by increasing the porosity, the critical buckling load parameter $\bar{P}_{cr}$ decreases because the plate stiffness decreases with the increase in porosity.

Moreover, the results presented in table 4 show that for $N > 1$ the porous FG plates with the porosity distribution

functions ψ_1 and ψ_2 have, respectively, the largest and the least critical buckling load. According to relation (3), it can be said that compared to E_c, volume fraction of the material E_m is more for the area above the mid-plane. Also, as can be observed from Fig 2, based on the function ψ_2, the more porosity distribution is seen for the area above the mid-plane whose material is more from E_m . However, based on the function ψ_3, the more porosity distribution is seen for the area below the mid-plane whose material is more from E_c. Since $E_c > E_m$ the plate stiffness for the distribution function of type 3 is greater than it for the distribution function of type 2. Also, for the distribution function of type 1, the same porosity is distributed symmetrically to the mid-plane. Therefore, we observe that the distribution porosity functions of types 1 and 2 lead to the most and the least critical buckling load, respectively.

Table 4. Effects of the porosity distribution, thickness ratio l_1/h, power-law index N and porosity φ, on the dimensionless critical buckling load parameter $\bar{P}_{cr} = P_{cr} l_2^2 / Eh^3$ for a square porous FG plate.

	l_1/h	φ	$N=0$	$N=1$	$N=2$	$N=5$	$N=10$
		0	30.0735	13.5487	9.2295	6.3834	5.4476
	5	0.2	27.3422	12.1799	8.2929	5.7490	4.9148
		0.5	22.9363	9.9833	6.7728	4.7034	4.0224
		0	35.9456	15.5979	10.6278	7.7997	6.9561
ψ_1	10	0.2	33.1414	14.1528	9.6404	7.1305	6.3906
		0.5	28.7977	11.8705	8.0643	6.0559	5.4696
		0	37.7923	16.2130	11.0501	8.2665	7.4790
	20	0.2	35.0012	14.7528	10.0534	7.5965	6.9164
		0.5	30.7740	12.4656	8.4756	6.5395	6.0215
		0	30.0735	13.5487	9.2295	6.3834	5.4476
	5	0.2	26.3778	11.9158	8.0946	5.5522	4.7492
		0.5	20.2916	9.2468	6.2532	4.2028	3.5987
		0	35.9456	15.5979	10.6278	7.7997	6.9561
ψ_2	10	0.2	31.5916	13.6875	9.2833	6.7429	6.0362
		0.5	24.2894	10.5345	7.0869	5.0136	4.4984
		0	37.7923	16.2130	11.0501	8.2665	7.4790
	20	0.2	33.2360	14.2184	9.6410	7.1334	6.4804
		0.5	25.5509	10.9173	7.3349	5.2752	4.8036
		0	30.0735	13.5487	9.2295	6.3834	5.4476
	5	0.2	26.3778	11.8124	8.0734	5.6324	4.7948
		0.5	20.2916	9.0266	6.2236	4.4086	3.7200
		0	35.9456	15.5979	10.6278	7.7997	6.9561
ψ_3	10	0.2	31.5916	13.6667	9.3616	6.9557	6.1842
		0.5	24.2894	10.5297	7.3107	5.5501	4.8768
		0	37.7923	16.2130	11.0501	8.2665	7.4790
	20	0.2	33.2360	14.2264	9.7539	7.3973	6.6718
		0.5	25.5509	10.9877	7.6464	5.9394	5.2914

Table 5. Effect of power-law index N and loading type conditions R on the dimensionless critical buckling load parameter $\bar{P}_{cr}$ of a square porous FG plate ($l_1/h=10$ and $\varphi=0.5$)

R		$N=0$	$N=1$	$N=2$	$N=5$	$N=10$
	ψ_1	28.7977	11.8705	8.0643	6.0559	5.4696
0	ψ_2	24.2894	10.5345	7.0869	5.0136	4.4984
	ψ_3	24.2894	10.5297	7.3107	5.5501	4.8768
	ψ_1	14.3988	5.9352	4.0321	3.0279	2.7348
1	ψ_2	12.1447	5.2673	3.5434	2.5068	2.2492
	ψ_3	12.1447	5.2648	3.6554	2.7751	2.4384
	ψ_1	53.1858$^{(2)}$	22.5842$^{(2)}$	15.3290$^{(2)}$	11.0150$^{(2)}$	9.6468$^{(2)}$
-1	ψ_2	46.0615$^{(2)}$	20.5136$^{(2)}$	13.8369$^{(2)}$	9.5172$^{(2)}$	8.3245$^{(2)}$
	ψ_3	46.0615$^{(2)}$	20.2497$^{(2)}$	14.0050$^{(2)}$	10.2317$^{(2)}$	8.7894$^{(2)}$

Table 5 shows the effects of the loading conditions on the critical buckling load of porous FG plates. This table shows that the porous FG plates, subjected to bi-axial tensile-compressive loading and bi-axial compressive loading, have the highest and the lowest critical buckling loads, respectively. This table also reveals that the buckling occurs at higher modes when the plate is subjected to bi-axial tensile-compressive loading.

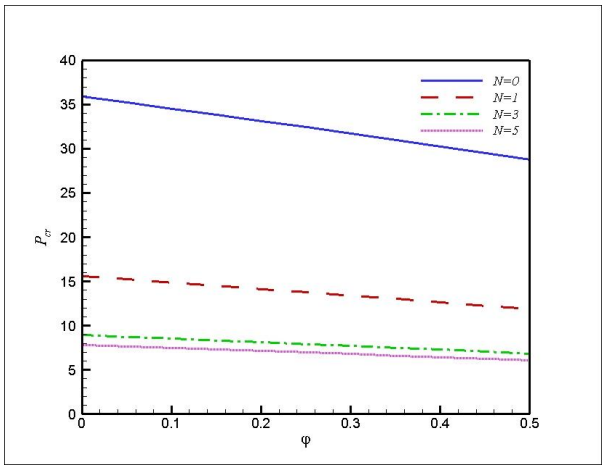

Fig 5. The dimensionless critical buckling load parameter $\bar{P}_{cr}$ of a square porous FG plate versus the porosity φ for the porosity distribution function type 1 ($l_1/h=10$)

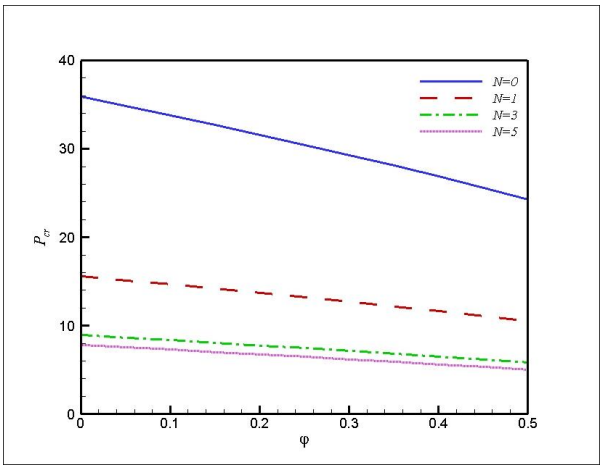

Fig 6. The dimensionless critical buckling load parameter $\bar{P}_{cr}$ of a square porous FG plate versus the porosity φ for the porosity distribution function type 2 ($l_1/h=10$)

The effect of the porosity φ on the critical buckling load parameter $\bar{P}_{cr}$ is illustrated in Fig 5 for different values of the power-law index N and the porosity distribution function of type 1. It can be seen from this figure that the critical buckling load parameter $\bar{P}_{cr}$ decreases almost linearly as the porosity φ increases. This issue, however, refers to the fact that the buckling load varies linearly with respect to the material properties. On the other hand, the material properties also vary linearly in relation to the porosity. Therefore, $\bar{P}_{cr}$ varies linearly with respect to φ. Furthermore, it is observed from this figure that by decreasing N, the porosity effect increases. Generally, by decreasing the power-law index N, volume fracture of the material with greater Young's modulus (E_c) increases and consequently the plate stiffness increases. Also, by decreasing the plate porosity, the plate stiffness increases. Therefore, it can be concluded that for smaller values of N, decreasing the porosity causes more stiffness for the plate. Consequently, the effect of the porosity should be more considerable for smaller values of N. Similar results are presented in Figs 6 and 7 for the porosity distribution functions of type 1 and 2, respectively.

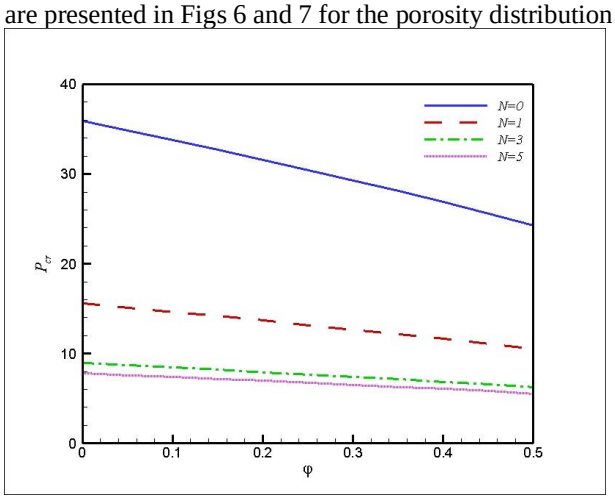

Fig 7. The dimensionless critical buckling load parameter $\bar{P}_{cr}$ of a square porous FG plate versus the porosity φ for the porosity distribution function type 3 ($l_1/h=10$)

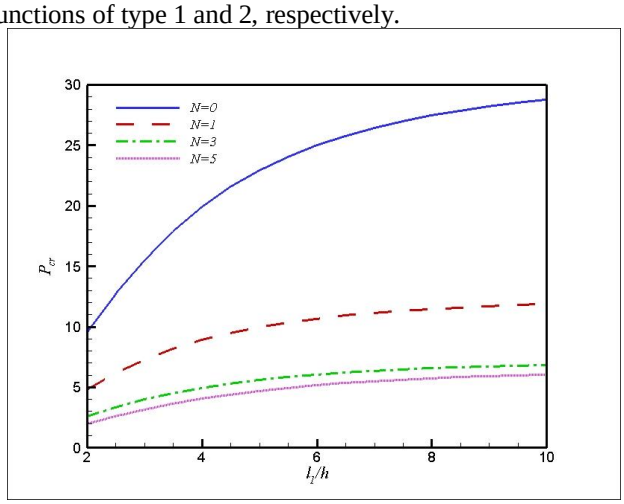

Fig 8. The dimensionless critical buckling load parameter $\bar{P}_{cr}$ of a square porous FG plate versus the thickness ratio l_1/h for the porosity distribution function type 1 ($\varphi=0.5$)

Figs 8, 9, and 10 illustrates $\bar{P}_{cr}$ in terms of the thickness ratio l_1/h for a square porous FG plate for various power-law index N values and different porosity distribution functions. As shown in these figures, by increasing the thickness ratio l_1/h, the critical buckling load parameter $\bar{P}_{cr}$ increases. These tables also show that the effect of the thickness ratio is more significant for the lower values of the power-law index N. Generally, by decreasing the

power-law index N , volume fracture of the material with greater Young's modulus (E_c) increases and consequently the plate stiffness increases. Furthermore, by increasing the plate thickness to length ratio, the plate stiffness increases. Therefore, it can be concluded that for smaller values of N , increasing the thickness causes more stiffness for the plate. Consequently, the effect of the thickness ratio should be more considerable for smaller values of N .

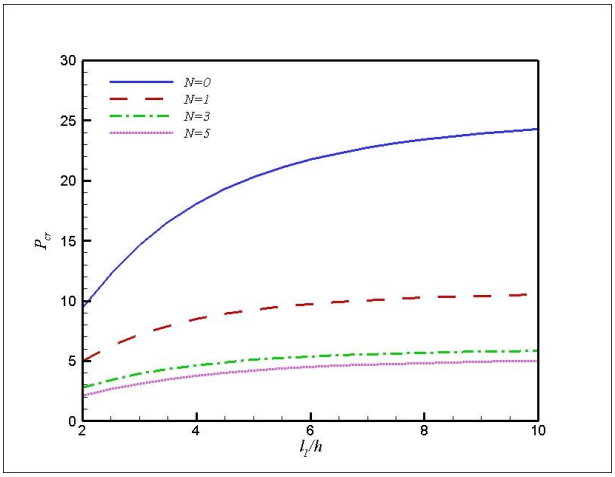

Fig 9. The dimensionless critical buckling load parameter $\bar{P}_{cr}$ of a square porous FG plate versus the thickness ratio l_1/h for the porosity distribution function type 2 ($\varphi = 0.5$)

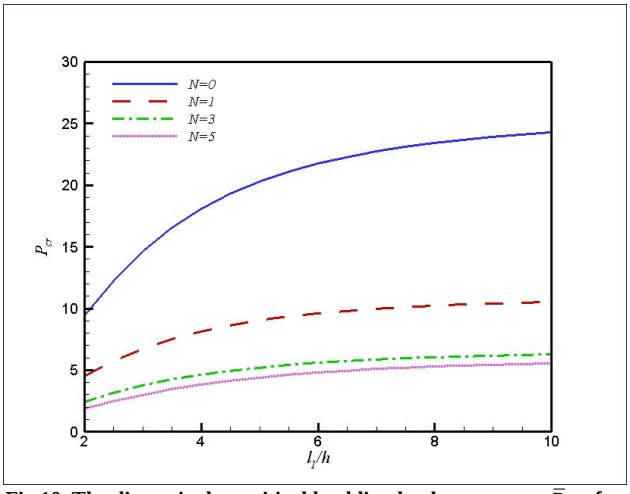

Fig 10. The dimensionless critical buckling load parameter $\bar{P}_{cr}$ of a square porous FG plate versus the thickness ratio l_1/h for the porosity distribution function type 3 ($\varphi = 0.5$)

Fig 11 shows the effect of the power-law index N for different values of φ and the porosity distribution function of type 1. Figs 12 and 13 show similar results for the porosity distribution function of types 2 and 3, respectively. These figures reveal that when the parameter N is increased, the critical buckling load decreases especially for small values of this parameter. It can be seen that for $N > 5$, the buckling load does not vary considerably by increasing the value of N .

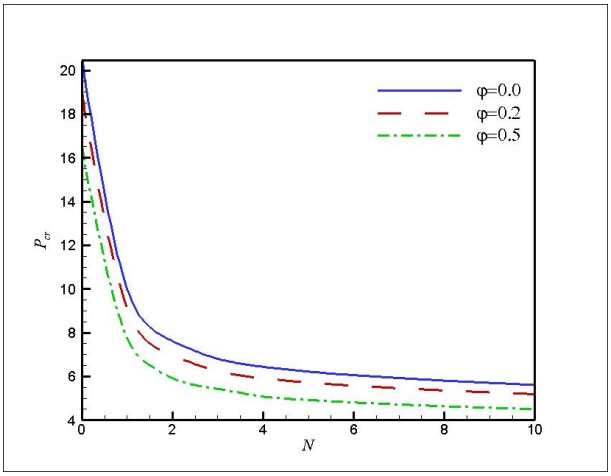

Fig 11. The dimensionless critical buckling load parameter $\bar{P}_{cr}$ of a square porous FG plate versus the power-law index N for the porosity distribution function type 1 ($l_1/h = 10$)

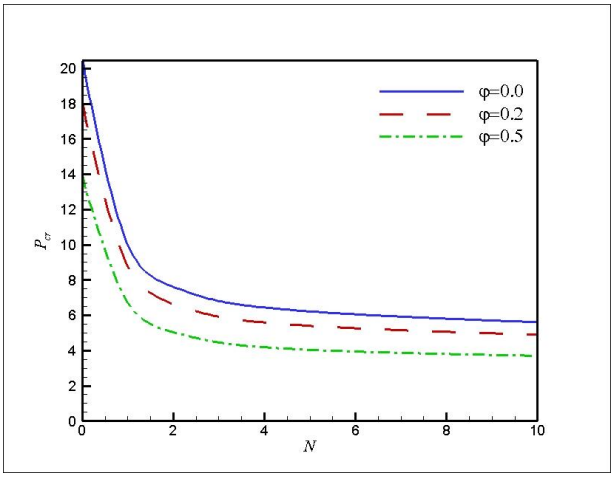

Fig 12. The dimensionless critical buckling load parameter $\bar{P}_{cr}$ of a square porous FG plate versus the power-law index N for the porosity distribution function type 2 ($l_1/h = 10$)

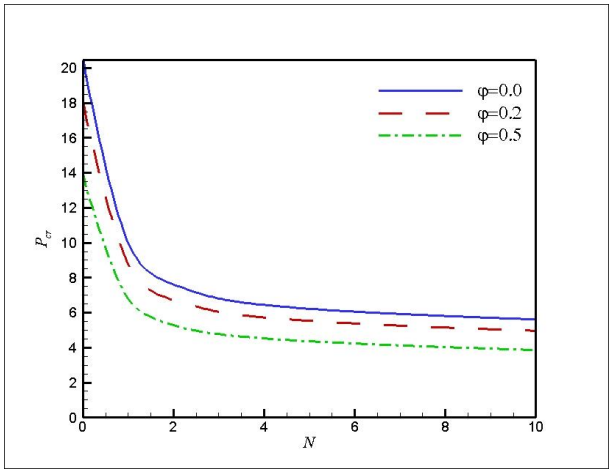

Fig 13. The dimensionless critical buckling load parameter of a square porous FG plate versus the power-law index for the porosity distribution function type 3.

9. Conclusion

This paper, studied buckling analysis of thick rectangular porous FG plates whose material and porosity distributions vary continuously along the thickness direction. Three types of porosity gradation along the thickness were considered. Since the material properties are asymmetry with respect to the mid-plane, it has been assumed that the in-plane loads are applied along its neutral plane, to eliminate the bending-stretching coupling. The governing stability equations were derived based on the higher-order shear and normal deformable plate theory and were solved analytically for rectangular plates with simple supports. To verify the results, the critical buckling load of the porous FG plate was obtained for the zero porosity factor and is then compared to those reported in the literature. Finally, the effects of different porosity distribution functions, porosity, power law index, thickness ratio, and loading condition have been investigated in detail on the critical buckling load of porous FG plates using HOSNDT. Also, the physical reasons of each effect have been discussed in detail. Some main results are listed below:

- The higher order shear and normal deformable plate theory presents more accurate results than the other theories of plate because of the accounting for all the possible plate deformations.
- The effect of HOSNDT is more important as the plate thickness increases.
- Compared to uniaxial load, the effect of HOSNDT is more considerable as the plate is subjected to a biaxial compression load.
- As the value of the power-law index increases, the critical buckling load and its sensitivity to that value decrease.
- By increasing the porosity, the critical buckling load decreases linearly.
- By decreasing the value of the power-law index, the effect of the porosity increases.
- Porous FG plates with type 1 and type 2 porosity distribution functions have the highest and least critical buckling load, respectively.
- Porous FG plates with symmetrical distribution of porosity to the mid-plane, behave stiffer than asymmetric pattern.
- The effect of the thickness ratio is more considerable for the smaller values of the power-law index.

References

[1] H. Altenbach, V. Rizov, Longitudinal Fracture Analysis of an Inhomogeneous Stepped Rod with Two Concentric Cracks in Torsion, *Technische Mechanik-European Journal of Engineering Mechanics,* Vol. 40, No. 2, pp. 149-159, 2020.

[2] V. Bhavar, P. Kattire, S. Thakare, R. Singh, A review on functionally gradient materials (FGMs) and their applications, in *Proceeding of,* IOP Publishing, pp. 012021.

[3] M. Choulaie, A. Bagheri, A. Khademifar, Nonlinear vibration and stability analysis of beam on the variable viscoelastic foundation, *Journal of Computational Applied Mechanics,* Vol. 48, No. 1, pp. 99-110, 2017.

[4] G. Udupa, S. S. Rao, K. Gangadharan, Functionally graded composite materials: an overview, *Procedia Materials Science,* Vol. 5, pp. 1291-1299, 2014.

[5] Y. Chen, F. W. Liou, Additive manufacturing of metal functionally graded materials: a review, 2018.

[6] D. Mahmoud, M. A. Elbestawi, Lattice structures and functionally graded materials applications in additive manufacturing of orthopedic implants: a review, *Journal of Manufacturing and Materials Processing,* Vol. 1, No. 2, pp. 13, 2017.

[7] F. Al Jahwari, A. A. Anwer, H. E. Naguib, Fabrication and microstructural characterization of functionally graded porous acrylonitrile butadiene styrene and the effect of cellular morphology on creep behavior, *Journal of Polymer Science Part B: Polymer Physics,* Vol. 53, No. 11, pp. 795-803, 2015.

[8] F. Al Jahwari, Y. Huang, H. E. Naguib, J. Lo, Relation of impact strength to the microstructure of functionally graded porous structures of acrylonitrile butadiene styrene (ABS) foamed by thermally activated microspheres, *Polymer,* Vol. 98, pp. 270-281, 2016.

[9] C. Han, Y. Li, Q. Wang, S. Wen, Q. Wei, C. Yan, L. Hao, J. Liu, Y. Shi, Continuous functionally graded porous titanium scaffolds manufactured by selective laser melting for bone implants, *Journal of the mechanical behavior of biomedical materials,* Vol. 80, pp. 119-127, 2018.

[10] I. T. Ozbolat, A. B. Khoda, Design of a new parametric path plan for additive manufacturing of hollow porous structures with functionally graded materials, *Journal of Computing and Information Science in Engineering,* Vol. 14, No. 4, pp. 041005, 2014.

[11] B. Goyal, A. Pandey, Critical review on porous material manufacturing techniques, properties & their applications, *Materials Today: Proceedings,* Vol. 46, pp. 8196-8203, 2021.

[12] I. Yadroitsev, I. Shishkovsky, P. Bertrand, I. Smurov, Manufacturing of fine-structured 3D porous filter elements by selective laser melting, *Applied Surface Science,* Vol. 255, No. 10, pp. 5523-5527, 2009.

[13] B. Koohbor, A. Kidane, Design optimization of continuously and discretely graded foam materials for efficient energy absorption, *Materials & Design,* Vol. 102, pp. 151-161, 2016.

[14] S. Giannitelli, F. Basoli, P. Mozetic, P. Piva, F. Bartuli, F. Luciani, C. Arcuri, M. Trombetta, A. Rainer, S. Licoccia, Graded porous polyurethane foam: A potential scaffold for oro-maxillary bone regeneration, *Materials Science and Engineering: C,* Vol. 51, pp. 329-335, 2015.

[15] F. Ebrahimi, F. Ghasemi, E. Salari, Investigating thermal effects on vibration behavior of temperature-dependent compositionally graded Euler beams with porosities, *Meccanica,* Vol. 51, pp. 223-249, 2016.

[16] A. Rezaei, A. Saidi, M. Abrishamdari, M. P. Mohammadi, Natural frequencies of functionally graded plates with porosities via a simple four variable plate theory: an analytical approach, *Thin-Walled Structures,* Vol. 120, pp. 366-377, 2017.

[17] Ş. D. Akbaş, Vibration and static analysis of functionally graded porous plates, *Journal of Applied and Computational Mechanics,* Vol. 3, No. 3, pp. 199-207, 2017.

[18] Y. Q. Wang, J. W. Zu, Large-amplitude vibration of sigmoid functionally graded thin plates with porosities, *Thin-Walled Structures,* Vol. 119, pp. 911-924, 2017.

[19] V. H. Nam, N. T. Phuong, D. T. Dong, N. T. Trung, N. V. Tue, Nonlinear thermo-mechanical buckling of higher-order shear deformable porous functionally graded material plates reinforced by orthogonal and/or oblique stiffeners, *Proceedings of the Institution of Mechanical Engineers, Part C: Journal of Mechanical Engineering Science,* Vol. 233, No. 17, pp. 6177-6196, 2019.

[20] J. Zhao, K. Choe, F. Xie, A. Wang, C. Shuai, Q. Wang, Three-dimensional exact solution for vibration analysis of thick functionally graded porous (FGP) rectangular plates with arbitrary boundary conditions, *Composites Part B: Engineering,* Vol. 155, pp. 369-381, 2018.

[21] A. G. Arani, Z. Khoddami Maraghi, M. Khani, I. Alinaghian, Free vibration of embedded porous plate using third-order shear deformation and poroelasticity theories, *Journal of Engineering,* Vol. 2017, 2017.

[22] S. Enayat, M. Hashemian, D. Toghraie, E. Jaberzadeh, A comprehensive study for mechanical behavior of functionally graded porous nanobeams resting on elastic foundation, *Journal of the Brazilian Society of Mechanical Sciences and Engineering,* Vol. 42, pp. 1-24, 2020.

[23] A. Rezaei, A. Saidi, On the effect of coupled solid-fluid deformation on natural frequencies of fluid saturated porous plates, *European Journal of Mechanics-A/Solids,* Vol. 63, pp. 99-109, 2017.

[24] A. Rezaei, A. Saidi, Exact solution for free vibration of thick rectangular plates made of porous materials, *Composite Structures,* Vol. 134, pp. 1051-1060, 2015.

[25] M. Askari, A. R. Saidi, A. S. Rezaei, M. A. Badizi, Navier-type free vibration analysis of porous smart plates according to reddy's plate theory, in *Proceeding of,* 13.

[26] A. R. Khorshidvand, A. R. Damercheloo, Bending, axial buckling and shear buckling analyses of FG-porous plates based on a refined plate theory, *Australian Journal of Mechanical Engineering,* Vol. 21, No. 2, pp. 705-724, 2023.

[27] V. Kumar, S. Singh, S. Harsha, Temperature dependent vibration characteristics of porous FG material plates utilizing FSDT, *International Journal of Structural Stability and Dynamics*, 2023.

[28] M. Arefi, S. Firouzeh, E. M.-R. Bidgoli, Ö. Civalek, Analysis of porous micro-plates reinforced with FG-GNPs based on Reddy plate theory, *Composite Structures,* Vol. 247, pp. 112391, 2020.

[29] A. Radwan, Quasi-3D integral model for thermomechanical buckling and vibration of FG porous nanoplates embedded in an elastic medium, *International Journal of Mechanical Sciences,* Vol. 157, pp. 320-335, 2019.

[30] S. Bathini, K. Vijaya Kumar Reddy, Flexural behavior of porous functionally graded plates using a novel higher order theory, *Journal of Computational Applied Mechanics,* Vol. 51, No. 2, pp. 361-373, 2020.

[31] Z. Zhou, Y. Wang, S. Zhang, R. Dimitri, F. Tornabene, K. Asemi, Numerical Study on the Buckling Behavior of FG Porous Spherical Caps Reinforced by Graphene Platelets, *Nanomaterials,* Vol. 13, No. 7, pp. 1205, 2023.

[32] M. Khatoonabadi, M. Jafari, F. Kiarasi, M. Hosseini, M. Babaei, K. Asemi, Shear buckling response of FG porous annular sector plate reinforced by graphene platelet subjected to different shear loads, *Journal of Computational Applied Mechanics,* Vol. 54, No. 1, pp. 68-86, 2023.

[33] K. Asemi, M. Babaei, F. Kiarasi, Static, natural frequency and dynamic analyses of functionally graded porous annular sector plates reinforced by graphene platelets, *Mechanics Based Design of Structures and Machines,* Vol. 50, No. 11, pp. 3853-3881, 2022.

[34] E. Arshid, S. Amir, A. Loghman, Bending and buckling behaviors of heterogeneous temperature-dependent micro annular/circular porous sandwich plates integrated by FGPEM nano-Composite layers, *Journal of Sandwich Structures & Materials,* Vol. 23, No. 8, pp. 3836-3877, 2021.

[35] M. Khatounabadi, M. Jafari, K. Asemi, Low-velocity impact analysis of functionally graded porous circular plate reinforced with graphene platelets, *Waves in Random and Complex Media,* pp. 1-27, 2022.

[36] M. Babaei, F. Kiarasi, K. Asemi, M. Hosseini, Functionally graded saturated porous structures: A review, *Journal of Computational Applied Mechanics,* Vol. 53, No. 2, pp. 297-308, 2022.

[37] K. Alhaifi, E. Arshid, A. R. Khorshidvand, Large deflection analysis of functionally graded saturated porous rectangular plates on nonlinear elastic foundation via GDQM, *Steel and Composite Structures, An International Journal,* Vol. 39, No. 6, pp. 795-809, 2021.

[38] M. Babaei, K. Asemi, Stress analysis of functionally graded saturated porous rotating thick truncated cone, *Mechanics Based Design of Structures and Machines,* Vol. 50, No. 5, pp. 1537-1564, 2022.

[39] M. Babaei, F. Kiarasi, K. Asemi, R. Dimitri, F. Tornabene, Transient thermal stresses in FG porous rotating truncated cones reinforced by graphene platelets, *Applied Sciences,* Vol. 12, No. 8, pp. 3932, 2022.

[40] A. Naderi, A. Saidi, On pre-buckling configuration of functionally graded Mindlin rectangular plates, *Mechanics Research Communications,* Vol. 37, No. 6, pp. 535-538, 2010.

[41] S. Coskun, J. Kim, H. Toutanji, Bending, free vibration, and buckling analysis of functionally graded porous micro-plates using a general third-order plate theory, *Journal of Composites Science,* Vol. 3, No. 1, pp. 15, 2019.

[42] J. Kim, K. K. Żur, J. Reddy, Bending, free vibration, and buckling of modified couples stress-based functionally graded porous micro-plates, *Composite Structures,* Vol. 209, pp. 879-888, 2019.

[43] D. Gilhooley, R. Batra, J. Xiao, M. McCarthy, J. Gillespie Jr, Analysis of thick functionally graded plates by using higher-order shear and normal deformable plate theory and MLPG method with radial basis functions, *Composite Structures,* Vol. 80, No. 4, pp. 539-552, 2007.

[44] M. Abdollahi, A. Saidi, M. Mohammadi, Buckling analysis of thick functionally graded piezoelectric plates based on the higher-order shear and normal deformable theory, *Acta Mechanica,* Vol. 226, No. 8, pp. 2497-2510, 2015.

[45] M. Bodaghi, A. Saidi, Levy-type solution for buckling analysis of thick functionally graded rectangular plates based on the higher-order shear deformation plate theory, *Applied Mathematical Modelling,* Vol. 34, No. 11, pp. 3659-3673, 2010.

[46] I. Ramu, S. Mohanty, Buckling analysis of rectangular functionally graded material plates under uniaxial and biaxial compression load, *Procedia Engineering,* Vol. 86, pp. 748-757, 2014.